Optimal Design of Handover Hybrid Energy Harvesting Based on Electric and Magnetic Fields

Chenjin Xu, Wei Wang, *Senior Member, IEEE*, Tianpeng Zhang, Jinchao Wang, and Yuchen Shi

***Abstract*—Electromagnetic field energy harvesting technology has garnered significant attention for its ability to power monitoring sensors without batteries. However, the magnetic field energy harvester (MFEH), despite its high power density, suffers from unstable energy output due to line current fluctuations, while the electric field energy harvester (EFEH) provides stable performance but limited energy capacity. To address these problems, a high-reliability combination and handover method for electromagnetic energy harvesting across a wide current operating range is proposed in this article. By integrating a pulsed-discharge EFEH winding into the single-winding magnetic core of a traditional MFEH, self-adaptive switching of the magnetic core operating state is achieved through coupling interactions between the electric and magnetic field windings. Under high line currents, this method effectively mitigates core saturation depth and suppresses voltage spikes. Under low line currents, it disconnects the electric field harvesting capacitor and elevates the output voltage to the load, ensuring sufficient power delivery. Experimental results validate the effectiveness and feasibility of the proposed method for hybrid electromagnetic energy harvesting, core saturation suppression, and load output voltage regulation.**

***Index Terms*—Core saturation suppression, coupled windings, current fluctuations, electromagnetic field hybrid power supply, voltage regulation.**

I. Introduction

POWER equipment monitoring sensors, as a core technology of new power systems, continue to develop toward multifunctional integration, flexibility, miniaturization, and low energy consumption. Driven by the digital transformation of power grids, monitoring sensors are widely deployed across power generation, transmission, substation, distribution, and consumption. Currently, most such monitoring sensors primarily rely on chemical batteries for power supply. However, due to problems such as high replacement costs, recycling difficulties, and disposal challenges, the extensive use of chemical batteries should be avoided. Fortunately, emerging ambient energy harvesting technologies have effectively resolved the challenge of providing green and sustainable power for monitoring sensors.

Monitoring sensors can be self-powered by harvesting scattered energy from the power equipment. Unlike photovoltaic (PV) [1], piezoelectric transducer (PZT) [2], or thermoelectric generator (TEG) [3], the self-powered energy harvesting is largely unaffected by external environmental variations, with magnetic field energy harvester (MFEH) [4] and electric field energy harvester (EFEH) [5] being the primary methods. EFEH harvests the high-voltage electric field around power lines. Due to the constant operating voltage of transmission lines, EFEH provides a stable power output. However, its energy harvesting capability is limited by μA-level charging currents in energy storage circuits. There is only weak capacitive coupling between power lines and energy harvesting systems, resulting in low energy extraction from electric fields. To address this challenge, a self-triggered pulsed-mode flyback converter was employed to transform a high-voltage dc bus rectified from the weakly coupled ac supply down to low voltage levels [6], [7]. On the basis of an instantaneous charging circuit, an upconversion oscillation circuit was proposed to achieve efficient electric-field energy. As a result, the instantaneous discharge circuit could output 110 mW to drive a wireless sensor node [8]. In [9], a multicapacitor cascaded configuration was adopted to enhance the power-to-current ratio (harvested power/displacement current) of EFEH, and an insulator leakage current monitoring system powered solely by EFEH was developed. For EFEH in HVDC systems, the absence of alternating electromagnetic fields makes it challenging to harvest energy for powering monitoring sensors. To address this, a bioinspired approach using natural leaves as electrodes was proposed, with experimental results demonstrating that the leaf-based EFEH device can drive ultralow-power sensors [10]. Meanwhile, a novel dc energy harvesting methodology that collects dc corona currents was introduced [11], offering a new pathway for self-powered monitoring in HVDC systems. In [12], a low-cost electric field energy harvesting was proposed, which can be integrated into an MV/HV asset-monitoring smart sensor.

Compared to EFEH, MFEH utilizes magnetic cores and energy harvesting windings to collect spatial magnetic energy for powering monitoring sensors. However, due to the wide current fluctuations in power lines, MFEHs face critical challenges: power supply dead zones under low currents and core saturation with voltage spikes under high currents. To address these problems, researchers have put forward a series of important

Received 19 August 2025; accepted 27 September 2025. Date of publication 1 October 2025; date of current version 23 December 2025. This work was supported in part by the National Nature Science Youth Foundation of China under Grant 51807095 and in part by the "333 Engineering" Research Project of Jiangsu Province under Grant 3-16-292. Recommended for publication by Associate Editor M. Ponce-Silva. *(Corresponding author: Wei Wang.)*

The authors are with the School of Electrical and Automation Engineering, Nanjing Normal University, Nanjing 210046, China (e-mail: 201001012@njnu.edu.cn; 61207@njnu.edu.cn; 241812160@njnu.edu.cn; 241802021@njnu.edu.cn; 231812063@njnu.edu.cn).

Color versions of one or more figures in this article are available at https://doi.org/10.1109/TPEL.2025.3616396.

Digital Object Identifier 10.1109/TPEL.2025.3616396

achievements in the optimization design of power windings and magnetic cores, as well as the design of magnetic field electric circuits [13], [14], [15], [16]. In the optimization of energy harvesting windings, a negative voltage feedback compensation control on the secondary winding of an MFEH to suppress core saturation was implemented [17]. Meanwhile, an active control winding with dynamically regulated currents was introduced, performing real-time magnetic flux modulation based on predicted saturation thresholds. This approach delivered 283 mW output power under 10 A/50 Hz primary current [18]. In the optimization of magnetic core design, a series capacitor is introduced into the MFEH circuit, extending the effective energy harvesting duration per cycle during core saturation [19]. Compared to conventional MFEH, this approach increased harvested power by 50%. In [20], adaptive power enhancement across varying line currents and loads by dynamically adjusting switching short-circuit intervals was achieved. Experimental results demonstrated a 206% power boost at 2 A power line current. Meanwhile, a low-power analog-controlled maximum power point tracking method was proposed in [21]. This solution achieved power improvements ranging from 101.39% to 149.89% under 1–10 A line currents. However, at low currents, the optimal load voltage becomes nonfixed and current-dependent. To resolve this, in [22], an adjustable input-voltage-reference MPPT circuit was designed, which enhanced harvesting power by 14% under low-current conditions. In the design of antisaturation circuits for MFEH, in [23], an energy management method based on critical saturation point tracking was proposed, which controls the output voltage at the critical saturation level under varying line currents, achieving simultaneous saturation suppression, maximum power point tracking, and adaptive energy management.

Obviously, MFEH is inherently susceptible to line current fluctuations. While existing researches focus on improving energy stability and power output under varying currents, critical challenges remain: persistent offline states of monitoring sensors during prolonged low currents and emergency energy cutoff during current surges. To address these limitations, the magnetic core of a dual-winding flyback transformer for hybrid EFEH and MFEH is reconfigured. By integrating MFEH and EFEH windings with controlled coupling, a hybrid circuit integration model is explored. Meanwhile, a wide current-range energy integration system is also established. Under high line currents, the core saturation depth is effectively reduced through counteractive flux generated by the EFEH winding, which suppresses voltage spikes. Under low line currents, it dynamically disconnects the EFEH capacitor, and the load output voltage can be elevated, ensuring sufficient power delivery to prevent load power shortages. The comparative analysis of energy harvesting capabilities is presented in Table I.

In Table I, compared to a single energy harvesting, multisource environment energy harvesting technology can provide more stable and efficient power. Furthermore, compared with ambient energy harvesting, the hybrid EFHE-MFEH system for harvesting electromagnetic field energy from power equipment demonstrates superior stability and efficiency.

TABLE I
COMPARATIVE ANALYSIS OF ENERGY HARVESTING CAPABILITIES

	Energy source	Power level	Stability	Power supply for circuits
[11]	EFEH	Milliwatt	Relatively stable	N/A
[24]	MFEH	Watt	Prone to core saturation	N/A
[25]	PZT+TEG	Milliwatt	Severely affected by environment	N/A
[26]	PZT+TEG+PV	Milliwatt	Severely affected by environment	N/A
This work	EFEH+MFEH	Milliwatt – Watt	Stable power harvesting with core saturation control	Self-powered

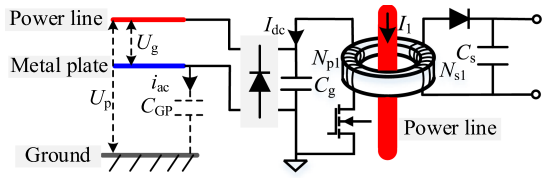

Fig. 1. EFEH based on the pulsed discharge method.

The remainder of this article is organized as follows: Section II discusses the feasibility analysis of electromagnetic hybrid energy harvesting integration. The model and simulation of the electromagnetic field handover hybrid energy harvesting integration are presented in Sections III and IV, respectively. Section V analyzes the integration and handover methodology for electromagnetic field energy harvesting across wide current operating ranges, which are verified by Section VI through experiments. Finally, Section VII presents a summary of the present work.

II. FEASIBILITY ANALYSIS OF ELECTROMAGNETIC HYBRID ENERGY HARVESTING INTEGRATION

Since EFEH provides only mW-level power, the load-driving capability of EFEH is inherently limited. Directly connecting the load to EFEH circuits cannot achieve a real-time energy supply. Therefore, EFEH is more suitable for intermittent load applications. Hence, this article adopts an intermittent EFEH. The EFEH, based on the pulsed discharge method, is introduced in Fig. 1.

In Fig. 1, I_1 represents the power line current. In the performance study of the EFEH circuit, it is initially assumed that I_1 equals zero. U_g and U_p denote the voltage between the power line and the ground and metal plate, the power line and the ground, respectively. C_g is defined as the capacitance value of the electric field energy harvesting capacitor (EFEHC). C_{GP} represents the equivalent capacitances between the metal plate and the ground. The displacement current i_{ac} flows through the metal plate-to-ground equivalent capacitance, while I_{dc} denotes the rectified charging current through the EFEHC. N_{p1} and N_{s1} are the winding turns on the primary and secondary sides of the magnetic core, respectively. The secondary side of the magnetic core supplies power to the load. In the EFEH circuit, C_s serves as the energy storage capacitor value at the load side. In Section V, this capacitor will serve as the rectifier capacitor and energy

storage capacitor for magnetic field energy harvesting, which can be called the magnetic field energy harvesting capacitor (MFEHC).

Then, the pulsed discharge approach charges the small-capacity EFEHC via displacement current. When the voltage of C_g reaches a specific threshold, the accumulated energy is released through a discharge switch and a pulse magnetic core to the C_s. The accumulated energy in the MFEHC is then regulated to power the load.

The performance-enhancing mechanism of the magnetic core in the EFEH is first examined. This step-down magnetic core ($N_{p1}>N_{s1}$) reduces the high voltage to levels suitable for high-capacity storage capacitors, while simultaneously amplifying the EFEHC discharge current for the MFEHC charging. The following is an analysis of the average power for the EFEH under two scenarios: directly powering loads and using a pulse discharge method.

A. Directly Powering Load

The EFEH drives the load directly, meaning the rectifier bridge is directly connected to the MFEHC. The energy stored in the MFEHC E_{m1} under direct electric field charging can be derived as follows:

$$E_{m1} = \frac{1}{2} C_s {U_s}^2 \tag{1}$$

where U_s denotes the voltage across the MFEHC, which is given by

$$U_s = \frac{I_{dc} t_s}{C_s} = \frac{0.9 I_{ac} t_s}{C_s} \tag{2}$$

where t_s is the time required to charge the MFEHC from 0 to the energy E_{m1}. I_{ac} represents the RMS value of the displacement current. Compared to the line voltage, the voltage between the metal plate and the high-voltage power line is much smaller than that between the high-voltage power line and the ground. Consequently, the RMS displacement current I_{ac} can be approximated by $\omega U_p C_{GP}$, where ω is the angular frequency. Therefore, assuming the voltage between the high-voltage power line and the ground remains constant, the RMS displacement current is maintained unchanged and can thus be treated as a constant current source. Hence, E_{m1} can be further represented as follows:

$$E_{m1} = \frac{(0.9 I_{ac} t_s)^2}{2C_s} = \frac{(0.9 \omega U_p C_{GP} t_s)^2}{2C_s}. \tag{3}$$

As derived from (3), given the constant U_P, ω, $C_{GP,}$ and t_s, reducing the C_s will result in a proportional increase in E_{m1} to maintain equality in (3).

B. Pulsed-Discharge Electric Field Energy Harvesting

Under pulsed-discharge electric field energy harvesting conditions, using the same time t_s to analyze the energy of the MFEHC during pulsed discharge, the energy stored in the MFEHC is denoted as E_{m2}. Note that the MFEHC is now connected to the secondary side of the magnetic core. Assuming zero losses in the magnetic core and circuitry during discharge, with no residual energy remaining after discharge and neglecting the millisecond-level discharge duration, the voltage U_g across the EFEHC, storing energy E_{m1} is derived from the principle of energy conservation as follows:

$$U_g = \sqrt{\frac{2E_{m1}}{C_g}}. \tag{4}$$

Therefore, when C_g remains constant, a higher U_g results in greater stored energy. However, U_g cannot be increased indefinitely due to the voltage ratings of the EFEHC, rectifier diode, and MOSFET. Similarly, if the same displacement current i_{ac} is directly used to charge the EFEHC, the energy of the EFEHC (same as the energy stored in the MFEHC) is expressed as follows:

$$E_{m2} = \frac{(0.9 I_{ac} t_s)^2}{2C_g} = \frac{(0.9 \omega U_p C_{GP} t_s)^2}{2C_g}. \tag{5}$$

By dividing (3) by (5)

$$\frac{E_{m1}}{E_{m2}} = \frac{C_g}{C_s}. \tag{6}$$

In (6), if $C_g << C_s$, then $E_{m2} >> E_{m1}$. It is thus clear that the energy in the MFEHC before and after implementing the pulsed-discharge method under the same charging time is much larger. Typically, the C_s is rated in thousands of microfarads, whereas the C_g is rated at several microfarads. Consequently, the pulsed-discharge electric field energy harvesting method substantially enhances the harvested energy. It is critically important to note in practical applications that C_g cannot be infinitely minimized, as this would cause U_g to increase; both the discharge MOSFET and EFEHC have specific voltage tolerance limits. Therefore, the discharge voltage of the EFEHC must be set below both the voltage rating of the EFEHC and the withstand voltage of the MOSFET.

As shown in Fig. 2(a), the simulation circuit for the pulsed discharge EFEH is configured with the following parameters: the transformer based on the magnetic core has a primary leakage inductance of 250 μH, magnetizing inductance of 1 H, and primary winding resistance and secondary winding resistance of

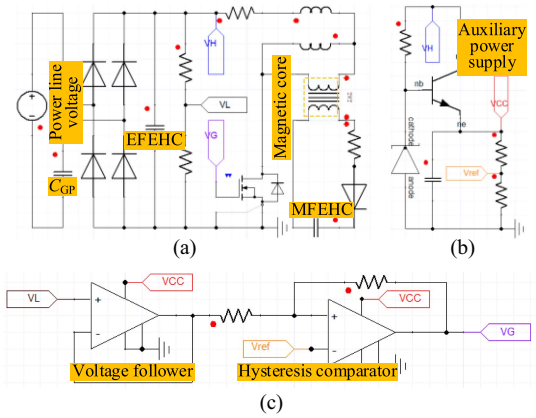

Fig. 2. Pulse discharge EFEH simulation circuit. (a) Main circuit. (b) Auxiliary power supply. (c) MOSFET drive circuit.

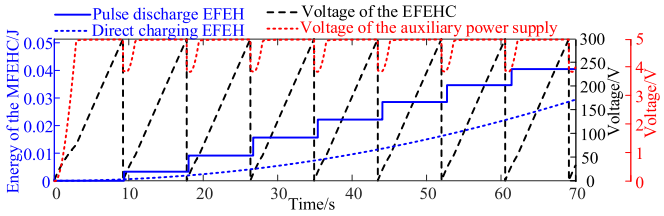

Fig. 3. Simulation waveforms.

12 and 2.4 Ω, respectively. The turns ratio of the transformer is $N_{p1}/N_{s1} = 550/90$. The phase voltage between the high-voltage power line and ground is 63.5 kV, the metal plate-to-ground equivalent capacitance is 6.1 pF, the EFEHC discharge voltage is 300 V, and the value of the MFEHC is 1000 μF. The auxiliary power supply circuit required for the MOSFET drive circuit is depicted in Fig. 2(b). A Zener diode stabilizes the input voltage within the tolerance range, and a transistor enhances the driving capability of the auxiliary power supply. MOSFET drive circuit itself, which employs a voltage follower and a hysteretic comparator to control the discharging of the EFEHC, is shown in Fig. 2(c). Note that the supply current of an operational amplifier is 1 μA.

The voltage waveforms of the EFEHC and auxiliary power supply under pulsed discharge are shown in Fig. 3. Meanwhile, the energy waveforms corresponding to the direct charging and pulse charging of the MFEHC are also presented to demonstrate the advantages of pulsed discharge EFEH, respectively.

In Fig. 3, the MOSFET is turned ON when the EFEHC reaches the preset threshold voltage, thereby discharging the MFEHC. The voltage of the auxiliary power supply can reach a stable value by the time of the next discharge of the EFEHC, indicating that the auxiliary power supply is feasible. By comparing the energy curves of the MFEHC under pulsed discharge and direct charging, it can be concluded that a greater amount of energy is harvested with the pulsed discharge approach. This also verifies the correctness of (6).

The key to hybrid energy harvesting from the electromagnetic field lies in ensuring simultaneous and interference-free energy harvesting from both paths. When power line current surges to thousands of amperes, the MFEH windings are short-circuited to protect the magnetic core from damage [27]. Conversely, when the current drops to single-digit amperes, MFEH output plummets sharply. Furthermore, the EFEH continues providing stable power to low-power monitoring sensors due to the stable power line voltage.

Hence, a hybrid electromagnetic field energy harvesting method is proposed in this article. The EFEH typically provides real-time power in the μW to mW range, while the MFEH operates in the mW to W range, revealing a significant disparity in energy harvesting capabilities between the two energy harvesting technologies. The pulsed-discharge EFEH circuit requires a flyback transformer to boost energy from weak capacitive coupling, whereas the noninvasive MFEH employs a clamped-on magnetic core that inherently functions as a specialized transformer. Therefore, there are inherent conditions

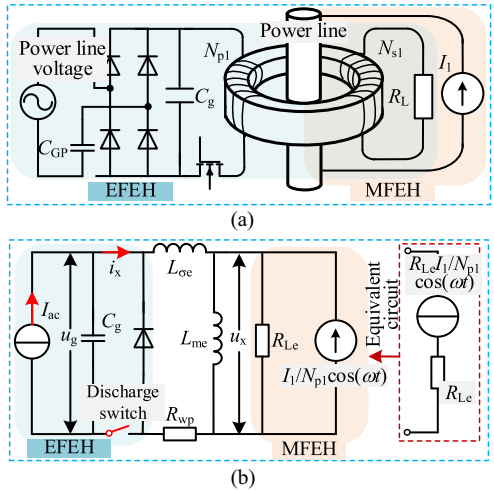

Fig. 4. Pulsed-discharge EFEH sharing a magnetic core with MFEH. (a) Schematic diagram. (b) Equivalent circuit.

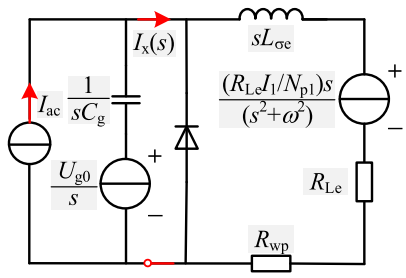

Fig. 5. Hybrid EFEH-MFEH complex frequency-domain equivalent circuit.

for the combination of pulse discharge EFEH and noninvasive MFEH.

The impact of integrating the power line winding (from MFEH) into a pulsed-discharge EFEH transformer is analyzed in this article. Fig. 4(a) and (b), respectively, illustrate the schematic diagram and equivalent circuit of a pulsed-discharge EFEH sharing a magnetic core with MFEH. In other words, three windings are wound on the transformer.

In Fig. 4(a), R_L denotes the equivalent load. In Fig. 4(b), R_{Le} denotes the reflected load resistance from the MFEH side to the EFEH winding side, calculated as $R_L {N_{p1}}^2/{N_{s1}}^2$. When the discharge switch is open, the rectified displacement current charges the EFEHC C_g to the discharge threshold voltage U_{g0}. Upon switch closure, the EFEHC connects to the reflected MFEH circuit, while the magnetizing inductance L_{me} is neglected. The resulting hybrid EFEH-MFEH complex frequency-domain equivalent circuit is depicted in Fig. 5.

In Fig. 5, since the rectified displacement current (I_{ac}) remains at the microampere level, which is significantly smaller than the reflected power line current. Hence, I_{ac} can be neglected when analyzing the transient of the EFEHC voltage during switch conduction. Based on the loop equation, the following equation can be obtained:

$$\left(\frac{1}{sC_g}+sL_{\sigma e}+R_{wp}+R_{Le}\right) I_x(s)=\frac{(R_{Le}I_1/N_{p1})s}{s^2+\omega^2}-\frac{U_{g0}}{s}. \tag{7}$$

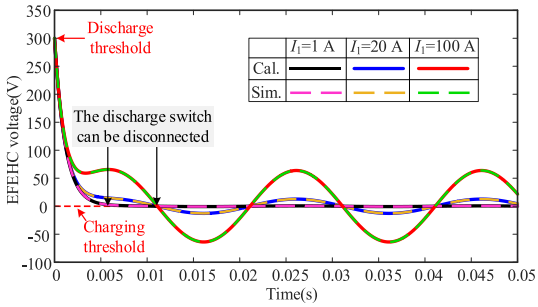

Fig. 6. Time domain waveform of the EFEHC.

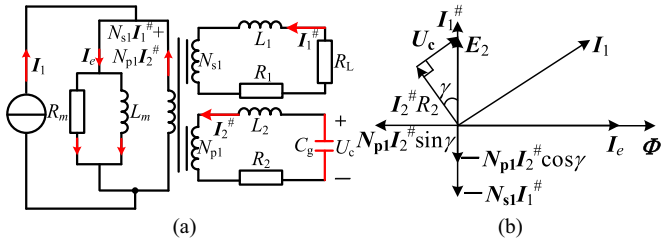

Fig. 7. Hybrid energy harvesting system. (a) Equivalent circuit. (b) Phasor diagram.

Furthermore, the expression for the loop current $I_x(s)$ can be obtained as follows:

$$I_x(s) = \frac{(R_{Le}I_1/N_{p1})s^2C_g/(s^2+\omega^2) - U_{g0}C_g}{1 + s^2L_{\sigma e}C_g + sC_gR_{wp} + sC_gR_{Le}}. \quad (8)$$

By applying the inverse Laplace transform to both sides of (8), the time-domain expression of the loop current can be derived. The voltage across the EFEHC is expressed as follows:

$$u_g(t) = \frac{1}{C_g}\int i_x(t)\mathrm{d}t, u_g(0_+) = u_g(0_-) = U_{g0}. \quad (9)$$

Assuming the pulse transformer of the EFEH has a primary leakage inductance of 250 μH, a primary winding resistance of 12 Ω, turns ratio N_{p1}/N_{s1} = 550/90, and a fixed magnetic field load of 10 Ω, with an electric field harvesting capacitor discharge voltage set to 300 V. It should be noted that the pulsed-discharge EFEH uses hysteresis comparator control to monitor the capacitor voltage thresholds (discharge threshold U_{g0} = 300 V, minimum threshold U_{g0} = 0 V) for cyclic charging. However, if the postdischarge voltage fails to reach the minimum threshold, the switch remains closed indefinitely, blocking displacement current from recharging the capacitor and rendering EFEH inoperative. Therefore, it is essential to analyze the voltage transient of the EFEHC after the discharge switch is closed and verify whether the charging threshold voltage of the EFEHC approaches 0 V. The time-domain calculation and circuit simulation waveforms of the EFEHC postdischarge are plotted in Fig. 6.

As shown in Fig. 6, the time required for the EFEHC to reach its charging threshold increases with rising line current. However, regardless of line current fluctuations, the EFEHC voltage consistently attains the charging threshold, ensuring the pulsed-discharge switch opens reliably to allow displacement current to recharge the EFEHC. This confirms the feasibility of sharing a magnetic core between pulsed-discharge EFEH and MFEH, with no interference to EFEH operation from MFEH integration.

To address the problem of MFEH being highly sensitive to line current fluctuations, this article proposes an innovative adaptive switching methodology that integrates EFEH as a supplemental power source during low-current conditions. The methodology achieves wide current-range compatibility through dynamic topology reconfiguration.

III. Electromagnetic Field Handover Hybrid Energy Harvesting Integration Model

The analysis begins with evaluating the load power supply characteristics of a multiwinding self-powered MFEH, where one winding is connected to a capacitive load (i.e., C_g) and the other to a resistive load (actual load). The equivalent circuit and corresponding phasor diagram of the hybrid energy harvesting system are illustrated in Fig. 7(a) and (b), respectively.

In Fig. 7(a), where I_e represents the magnetizing current. $I_1{}^{\#}$ and $I_2{}^{\#}$ denote the currents flowing through the MFEH winding and EFEH winding. R_1 and L_1 are the internal resistance and leakage inductance of the MFEH winding, respectively. R_2 and L_2 are the internal resistance and leakage inductance of the EFEH winding, respectively. The voltage across the EFEHC is U_c. The voltage of the EFEH winding denotes E_2. On the current-carrying conductor side, R_m and L_m represent the magnetizing resistance and the magnetizing inductance, respectively. According to the law of conservation of magnetomotive force

$$\boldsymbol{I}_1 = N_{s1}\boldsymbol{I}_1{}^{\#} + N_{p1}\boldsymbol{I}_2{}^{\#} + \boldsymbol{I}_e. \quad (10)$$

The main magnetic flux Φ in the magnetic core is influenced by the magnetizing current I_e, which is constrained by the magnetomotive force I_1, $N_{s1}I_1{}^{\#}$, and $N_{p1}I_2{}^{\#}$. This indicates that an interaction mechanism exists between the main magnetic flux and the fluxes in both the EFEH and MFEH windings.

By assuming a high-permeability magnetic core and neglecting magnetizing resistance, secondary leakage inductances L_1 and L_2, the induced voltages $e_1(t)$ (MFEH winding) and $e_2(t)$ (EFEH winding) are derived from Faraday's law of electromagnetic induction

$$\begin{cases} e_1(t) &= -N_{s1}\mathrm{d}\Phi/\mathrm{d}t = -N_{s1}d\left(\int_{r_1}^{r_2}\frac{\mu\sqrt{2}I_e\cos\omega t}{2\pi\rho}\mathrm{d}\rho\int_0^h \mathrm{d}h\right)/\mathrm{d}t \\ &= \sqrt{2}N_{s1}\mu f h\ln\frac{r_2}{r_1}I_e\sin\omega t \\ e_2(t) &= -N_{p1}\mathrm{d}\Phi/\mathrm{d}t == \sqrt{2}N_{p1}\mu f h\ln\frac{r_2}{r_1}I_e\sin\omega t \end{cases} \quad (11)$$

where r_1, r_2, and h are the inner radius, outer radius, and height of the magnetic core, μ is the magnetic permeability, and f denotes the frequency of the line current, $\omega = 2\pi f$. In addition, the currents flowing through the MFEH winding and the EFEH

winding are, respectively, represented as follows:

$$\begin{cases} {I_1}^{\#} = \frac{E_1}{R_1+R_\mathrm{L}} = \frac{N_{\mathrm{s}1}\mu f h \ln(r_2/r_1) I_e}{R_1+R_\mathrm{L}} = \Gamma_1 I_\mathrm{e} \\ {I_2}^{\#} = \frac{E_2}{|R_2+1/j\omega C_\mathrm{g}|} = \frac{N_{\mathrm{p}1}\mu f h \ln(r_2/r_1) I_e}{\sqrt{{R_2}^2+(1/\omega C_\mathrm{g})^2}} = \Gamma_2 I_e \\ \Gamma_1 = \frac{N_{\mathrm{s}1}\mu f h \ln(r_2/r_1)}{R_1+R_\mathrm{L}} \\ \Gamma_2 = \frac{N_{\mathrm{p}1}\mu f h \ln(r_2/r_1)}{\sqrt{{R_2}^2+(1/\omega C_\mathrm{g})^2}} \end{cases}. \quad (12)$$

In (12), both ${I_1}^{\#}$ and ${I_2}^{\#}$ can be expressed in terms of I_e. In practice, the value of I_1 can be measured. Therefore, ${I_1}^{\#}$, ${I_2}^{\#}$, and I_e all need to be expressed in terms of I_1. Furthermore, γ can be calculated as follows:

$$\gamma = \arctan(\omega C_\mathrm{g} R_2)^{-1}. \quad (13)$$

γ is the angle between ${I_2}^{\#}$ and ${I_1}^{\#}$. Next, in Fig. 7(b), according to the Pythagorean Theorem, the following equation can be obtained:

$$\left(I_e - N_{\mathrm{p}1}{I_2}^{\#}\sin\gamma\right)^2 + \left(N_{\mathrm{s}1}{I_1}^{\#} + N_{\mathrm{p}1}{I_2}^{\#}\cos\gamma\right)^2 = {I_1}^2. \quad (14)$$

The relationship between the magnetizing current I_e and the line current I_1 can be expressed as follows:

$$\begin{cases} I_\mathrm{e} = \dfrac{I_1}{\sqrt{\begin{array}{l}1 - 2N_{\mathrm{p}1}\Gamma_2\sin\gamma + (N_{\mathrm{p}1}\Gamma_2\sin\gamma)^2 + \\ {N_{\mathrm{s}1}}^2{\Gamma_1}^2 + 2N_{\mathrm{s}1}N_{\mathrm{p}1}\Gamma_1\Gamma_2\cos\gamma + (N_{\mathrm{p}1}\Gamma_2\cos\gamma)^2\end{array}}} \\ \quad = \Gamma_3 I_1 \\ \Gamma_3 = [1 - 2N_{\mathrm{p}1}\Gamma_2\sin\gamma + {N_{\mathrm{s}1}}^2{\Gamma_1}^2 + 2N_{\mathrm{s}1}N_{\mathrm{p}1}\Gamma_1\Gamma_2\cos\gamma \\ \quad + (N_{\mathrm{p}1}\Gamma_2)^2]^{-1/2} \end{cases}. \quad (15)$$

Combining (12) and (15), it can be seen that ${I_1}^{\#}$, ${I_2}^{\#}$, and I_e can all be expressed in terms of I_1. Hence, the output voltage U_L and power P across the load R_L can be expressed as follows:

$$\begin{cases} U_\mathrm{L} = {I_1}^{\#} R_\mathrm{L} = \Gamma_1 I_e R_\mathrm{L} = \Gamma_1\Gamma_3 I_1 R_\mathrm{L} \\ P = \left({I_1}^{\#}\right)^2 R_\mathrm{L} = (\Gamma_1 I_e)^2 R_\mathrm{L} = {\Gamma_1}^2{\Gamma_3}^2{I_1}^2 R_\mathrm{L} \end{cases}. \quad (16)$$

Furthermore, according to Ampere's Loop Theorem

$$Hl = \sqrt{2} I_\mathrm{e}. \quad (17)$$

Therefore, the magnetic field intensity of the magnetic core can be expressed as follows:

$$H = \frac{\sqrt{2} I_1 \Gamma_3 C_\mathrm{g}}{\pi(r_1+r_2)}. \quad (18)$$

The abovementioned analysis establishes the analytical relationships between the output voltage, output power, magnetic field intensity, and variables including line current, load resistance, and EFEHC capacitance. From (16), the induced voltage of the MFEH winding (i.e., the input voltage of the buck converter) increases with rising line current. Due to the constant-power characteristic of the load, the input current of the buck converter decreases proportionally, causing the equivalent load impedance to rise as the power line grows. Equation (18) further reveals that increases in either load impedance or line current drive the magnetic core toward saturation. Meanwhile, in (18), the value of Γ_3 is related to the capacitance of EFEHC, thus the magnetic field intensity of the core can be adjusted by regulating the value of C_g. When the core enters saturation, the output power during one cycle under saturated conditions can be further expressed as follows:

$$\begin{aligned} P_{\mathrm{r-sat}} &= \frac{2}{T}\int_0^{t_\mathrm{s}} \left[{i_1}^{\#}(t)\right]^2 R_\mathrm{L}\mathrm{d}t \\ &= \frac{2{I_1}^2{\Gamma_1}^2{\Gamma_3}^2 R_\mathrm{L}}{\pi}\int_0^{t_\mathrm{s}} [\cos(\omega t)]^2 \mathrm{d}(\omega t) \\ &= \frac{{I_1}^2{\Gamma_1}^2{\Gamma_3}^2 R_\mathrm{L}}{\pi}\left[\omega t_\mathrm{s} + \frac{1}{2}\sin(2\omega t_\mathrm{s})\right]. \end{aligned} \quad (19)$$

The parameter t_s represents the effective energy transfer time during half-cycle operation of the core in saturated states. According to Faraday's law of electromagnetic induction, it can be derived that

$$\int_0^{t_\mathrm{s}} [{i_1}^{\#}(t)(R_1+R_\mathrm{L})]\mathrm{d}t = N_{\mathrm{s}1}(r_2-r_1)h\int_0^{t_\mathrm{s}} \mathrm{d}B(t) \quad (20)$$

then t_s can be expressed as follows:

$$t_\mathrm{s} = \min\left[\frac{1}{\omega}\sin^{-1}\left(\frac{(r_2-r_1)N_{\mathrm{s}1}hB_{\mathrm{sat}}\omega}{\sqrt{2}\Gamma_1\Gamma_3 I_1(R_\mathrm{L}+R_1)}\right), \frac{T}{2}\right]. \quad (21)$$

Therefore, combining with (19), the final output power of magnetic field energy harvesting can be achieved in both saturated and nonsaturated operating states.

IV. Electromagnetic Field Handover Hybrid Energy Harvesting Integration Simulation

The magnetic core dimensions are defined with an inner radius of 20 mm, outer radius 40 mm, height $h = 25$ mm, and wire diameter 0.1 mm. The initial permeability of the magnetic core, called 1K107, is 100000. The winding turns for EFEH and MFEH are 300 turns and 100 turns, respectively. The power line current is 10 A. Finite element simulations are performed using coupled with circuit cosimulation to evaluate variations in load voltage, output power, and magnetic field intensity versus the EFEHC capacitance, under different load resistances. The results are plotted in Fig. 8(a) and (b).

In Fig. 8(a) and (b), the simulated magnetic field intensity represents the magnetic field strength on the neutral axis of the core. Notably, the simulated magnetic field intensity is slightly greater than the calculated value, but both exhibit the same trend of variation with the EFEHC capacitance. Meanwhile, the magnetic field intensity variation range with EFEHC for $R_\mathrm{L} = 10\ \Omega$ is significantly smaller compared to $R_\mathrm{L} = 100\ \Omega$. Additionally, the load voltage and output power are more sensitive to changes in the EFEHC capacitance. Meanwhile, as the EFEHC capacitance continues to increase, the load voltage, output power, and magnetic field strength decrease very gently in the initial stage. As the EFEHC capacitance continues to increase, the load output voltage and magnetic field intensity sharply decrease, and the load voltage, output power, and magnetic field strength are positively correlated with the line current, and do not affect the trend of changes in load voltage, output power, and magnetic field intensity caused by the increase in EFEHC capacitance. Therefore, by coupling the double windings wound on the

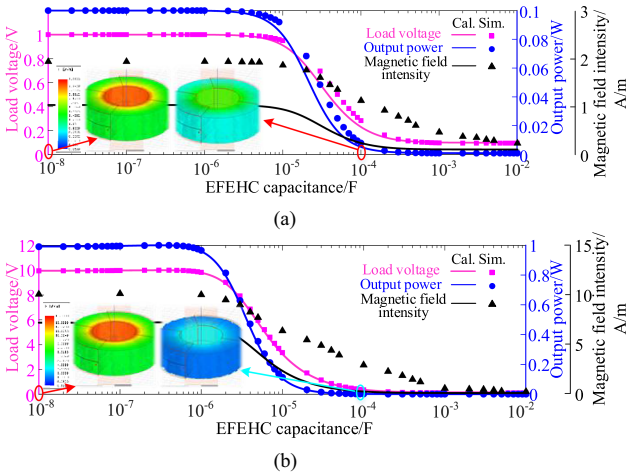

Fig. 8. Influence curve of the EFEHC capacitance. (a) $R_{\mathrm{L}} = 10\ \Omega$. (b) $R_{\mathrm{L}} = 100\ \Omega$.

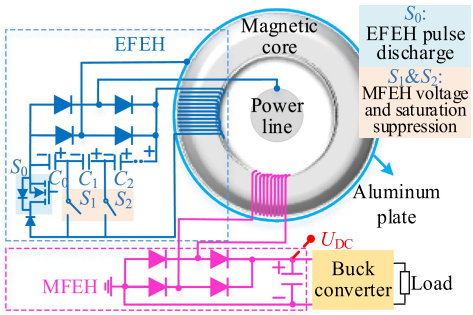

Fig. 9. Schematic diagram of electromagnetic field handover hybrid energy harvesting integration.

magnetic core, the EFEHC capacitor can effectively regulate parameters such as load voltage, output power, and the working range of the magnetic core.

V. Integration and Handover Methodology for Electromagnetic Field Energy Harvesting

The abovementioned analysis demonstrates that selecting an appropriate EFEHC effectively reduces the magnetic field intensity within the core, thereby preventing core saturation. Moreover, the continuous increase in the EFEHC capacitance also effectively suppresses voltage surges in the load. This prevents the input voltage of the buck converter from exceeding its maximum tolerance.

By reusing EFEHC energy storage and energy allocation functions, an adaptive integration and handover methodology for electromagnetic field energy harvesting for wide current-range operation is proposed. As shown in Fig. 9, the hybrid electromagnetic energy harvesting circuit integrates both EFEH and MFEH mechanisms on a shared toroidal high-permeability magnetic core. Notably, the rectifier capacitor that connects the MFEH is still called the MFEHC as expected.

Furthermore, the EFEHC consists of multiple series-connected capacitors, each equipped with an ac switch connected to the EFEH winding. This configuration achieves dual objectives: enhancing voltage tolerance for high-voltage energy harvesting and enabling adaptive magnetic core regulation by dynamically adjusting the capacitive through ac switch operation. Meanwhile, the MFEHC not only stabilizes and rectifies the load voltage, but also stores energy for both magnetic and electric field energy. To achieve a stable power supply across wide current fluctuations, the critical limitations of conventional MFEH (low-current deficiency, high-current hazards) can be solved by this design.

This article ensures the magnetic-induced voltage remains below the maximum input threshold of the buck converter while reducing core saturation under high line currents. By adaptively adjusting the number of EFEHC based on the voltage of the MFEHC. Based on the coupling effects between MFEH and EFEH windings, three key functions can be achieved: low-current electric field energy supplementation, high-current core saturation suppression, and self-powered operation without external power intervention. Set $U_{\mathrm{dc,min}}$, and $U_{\mathrm{dc,max}}$ as the minimum voltage and maximum voltage input of the buck converter, and U_{dc} is denoted as the input voltage of the buck converter.

Under minimal line current conditions, the EFEH, sharing a magnetic core with the MFEH, provides intermittent power to the load via pulsed discharge. When the line current increases, the MFEH resumes energy supply as the magnetic energy meets the load demand. In this state, the EFEHC acts as an energy diversion component. Based on the input voltage U_{dc} of the buck converter, the load power source is selected from two charging modes:

1) *EFEH Power Supply:* $U_{\mathrm{dc}} < U_{\mathrm{dc,min}}$

When the power line current is extremely low, the MFEH cannot reach the buck converter startup threshold voltage. In this state, switch S_0 operates as a pulsed discharge controller for electric field energy, adopting a "short-term high level, long-term low level" switching pattern. The EFEH elevates the voltage of the MFEHC through pulsed discharge cycles.

2) *MFEH Power Supply:* $U_{\mathrm{dc,min}} < U_{\mathrm{dc}} < U_{\mathrm{dc,max}}$

Normally, when the power line current increases or the equivalent load rises, the input voltage U_{dc} of the buck converter gradually increases. Once U_{dc} exceeds the startup threshold ($U_{\mathrm{dc,min}}$), the load power source switches from the EFEH to the MFEH. However, as the power line current continues to rise, U_{dc} may exceed the buck converter maximum tolerance voltage $U_{\mathrm{dc,max}}$. To address this, this article employs stepwise adjustment of the EFEHC capacitance to adaptively divert excess magnetic energy and dynamically regulate U_{dc}, ensuring reliable electromagnetic energy harvesting and stable power supply across wide-ranging power line current variations.

Based on the aforementioned analysis, this article presents the electromagnetic field energy harvesting handover schematic diagram shown in Fig. 10.

As shown in Fig. 10, the minimum (startup threshold) voltage and maximum input voltage of the buck converter selected by the voltage regulator module are first determined. If the input voltage under varying line current is below the startup threshold, the magnetic field energy cannot directly power the load, and pulsed EFEH is employed to supply the load; if the input voltage exceeds the startup threshold but remains below the maximum

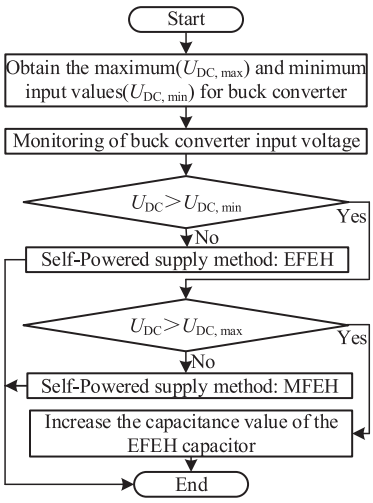

Fig. 10. Electromagnetic field energy harvesting handover schematic diagram.

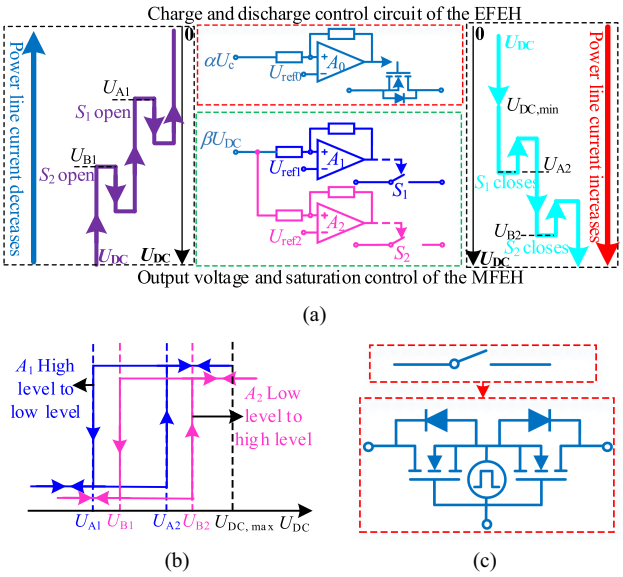

Fig. 11. EFEH charge-discharge control and MFEH saturation adaptive control circuit. (a) Hysteresis comparator-based switch control schematic. (b) Hysteresis comparator output level diagram. (c) AC switch structure.

input threshold, MFEH is employed to provide real-time energy to the load; if the line current continues to increase, causing the buck converter input voltage to exceed the threshold, the EFEHC is increased to reduce the internal magnetic field intensity of the core, thereby lowering the buck converter input voltage to protect the magnetic core.

The EFEHC, composed of three series-connected capacitors, is illustrated in Fig. 11(a), which shows the charge-discharge control circuit of the EFEH and the core saturation control circuit of the MFEH. Here, α and β are the voltage division coefficients of the EFEH capacitors, with αU_c and βU_{dc} representing the divided voltages of the EFEH and MFEH capacitors after resistive division. Hysteresis comparator A_0 controls the pulsed discharge of the EFEH, while A_1 and A_2 govern switches S_1 and S_2, respectively, with reference voltages U_{ref0}, U_{ref1}, and U_{ref2}. The thresholds follow $U_{dc,min}<<U_{A1}<U_{B1}<U_{A2}<U_{B2}<U_{dc,max}$. Fig. 11(b) visually depicts the voltage hysteresis diagrams of the comparator outputs under core saturation control, intuitively showing their level transitions. Switches S_1 and S_2 in Fig. 11(a) are implemented as back-to-back MOSFET ac switches (structural details in Fig. 11(c)).

Fig. 11(a) demonstrates that under extremely low line current conditions, the EFEH serves as the primary power source for the load. When the line current increases and the load voltage U_{dc} exceeds $U_{dc,\,min}$, the primary power source transitions from the EFEH to the MFEH. As the line current continues to rise and U_{dc} reaches U_{A2}, hysteresis comparator A_1 outputs a high-level signal to activate switch S_1, reducing the capacitance of the EFEHC from three (C_1//C_2//C_3) to two (C_1//C_2). This lowers the equivalent capacitance, causing U_{dc} to drop sharply if the line current remains constant, according to Section IV. When the current further increases, U_{dc} recovers until it exceeds U_{A2} and reaches U_{B2}, triggering hysteresis comparator A_2 to activate switch S_2, leaving only C_2 in the EFEH circuit and further reducing U_{dc}. Conversely, as the line current decreases and U_{dc} falls below U_{A2} and U_{A1}, switches S_2 and S_1 sequentially close, resulting in a stepwise decline of U_{dc}. This mechanism defines the configuration method for EFEHC parameters to achieve adaptive voltage regulation. The specific steps are as follows.

1) When the line current increases from zero and U_{dc} reaches U_{A2}, switch S_1 is closed, and the EFEHC form a parallel configuration (C_1//C_2). To ensure stable operation of the buck converter, the load voltage must satisfy $U_{A1}<U_{dc}(C_1, C_2)<U_{A2}$.
2) As the line current continues to rise and the MFEHC voltage exceeds U_{A2} to U_{B2}, switch S_2 is closed, reducing the capacitance to C_2. For reliable operation of the hybrid electromagnetic energy harvesting system, the load voltage must meet $U_{B1}<U_{dc}(C_2)<U_{B2}$.

VI. Experimental Verification

To achieve efficient electromagnetic energy integration across wide current ranges, voltage references, operational amplifiers, and other energy-consuming electronic components are required. Direct use of external batteries or power sources contradicts the self-powered design principle of the monitoring sensors. Therefore, while selecting ultralow-power electronic components, a stable auxiliary power supply under wide-ranging line current fluctuations remains critical for reliable operation of the hybrid electromagnetic energy harvesting circuit. The EFEH auxiliary power circuit shown in Fig. 2(b) is also adopted. When $U_{dc}<U_{dc,min}$(i.e., the EFEH acts as the primary power source), the EFEH auxiliary power supply stably powers the voltage references and operational amplifiers on the electric field side. When $U_{dc}>U_{dc,min}$ and the MFEH becomes the primary power source, continuing to use the EFEH auxiliary power for U_{dc}-monitoring electronics would place the gates of switches S_1, S_2, and S_0 at the same potential, risking system instability. Therefore, the EFEH auxiliary power is copied to the MFEH

TABLE II
EXPERIMENTAL PARAMETERS

Parameters	Value
Inner radius/outer radius/height of magnetic core	20 mm/40 mm/25 mm
Core material	1K107
MFEHC	2200 μF
$C_0/C_1/C_2$	12 μF/100 μF/100 μF
Discharge voltage	300 V
Load resistance	150 Ω
MFEH winding / EFEH winding	90 /550
BJT	KSC5027
Zener	MMSZ4691
Voltage reference	ISL60002 (Quiescent current :350 nA)
Operational amplifier	TLV3691 (Quiescent current :75 nA)
Rectifier diode	IDM02G120C5 (Reverse current: 1.2 μA)
MOSFET	IRFP460 (Drain-source leakage current: 2 μA)

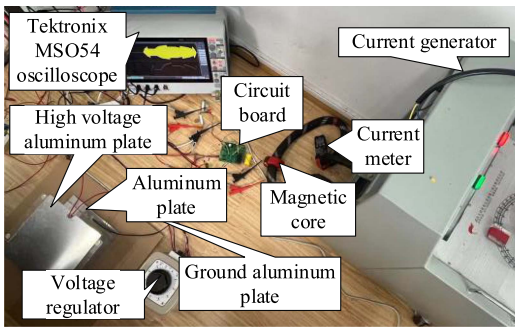

Fig. 12. Experiment platform.

side and parallel-connected to the MFEH capacitor, providing power to the $U_{\rm dc}$-monitoring electronics.

A. Experimental Platform

Taking the LTC7131-1 buck converter IC (input voltage range: 4.5–20 V) as an example, the auxiliary power supply requires the voltage across the MFEHC to exceed the 5.6 V Zener diode stabilization voltage for stable operation. In experiments, the hysteresis thresholds are set to $U_{\rm A1} = 7.5$ V, $U_{\rm B1} = 10.2$ V, $U_{\rm A2} = 14.6$ V, and $U_{\rm B2} = 17.8$ V. The experimental parameters are listed in Table II. When the energy-harvesting core operates as a pulsed discharge transformer, its primary leakage inductance is 15.75 mH, magnetizing inductance is 370 mH, with winding resistances of 159.7 Ω (EFEH) and 5.1 Ω (MFEH).

In Table II, the voltage reference is employed for the cathode input of the hysteresis comparator. Based on the auxiliary power supply consumption and MOSFET leakage current, the $I_{\rm dc}$ in Fig. 1 must be at least 3.7 μA. As shown in Fig. 12, the experimental platform employs a three-electrode configuration to simulate the EFEH environment: the top aluminum plate simulates the high-voltage power line, the middle aluminum plate acts as the practical EFEH plate, and the bottom aluminum plate represents the ground. The voltage regulator connects the top and bottom plates, while the top and middle plates are linked

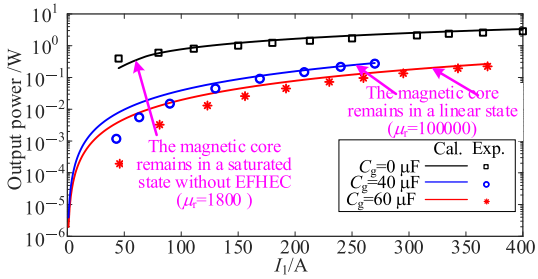

Fig. 13. Variation of output power with current.

to the EFEH circuit. The current value from the current generator is measured via a clamp meter, and the voltage waveforms of the MFEH winding and load voltage are recorded using a high-precision oscilloscope.

B. Experimental Results

First, the variation of the output power of the MFEH with the line current is analyzed. The magnetic core is continuously influenced by the change in the power line current. Therefore, the calculation of the output power of the magnetic core is divided into two intervals. When the magnetic core is not saturated, the relative permeability of the magnetic core is still set to 100000. When the magnetic core enters the saturation state, the maximum saturation magnetic flux density of the magnetic core is 1.2 T. Taking a line current of 100 A as an example, based on Ampere's law, the relative permeability can be calculated as follows:

$$\mu_r = \frac{B}{H\mu_0} = \frac{B\pi(r_1 + r_2)}{\mu_0 I_1}. \tag{22}$$

where B denotes the magnetic flux density, and $\mu_{\rm r}$ and μ_0 are the relative permeability of the magnetic core and vacuum permeability, respectively. Hence, the value of $\mu_{\rm r}$ is calculated to be 1800. Therefore, it is assumed that the permeability of the magnetic core in the saturated state is 1800 for the purpose of calculation. The experimental and calculated results are presented in Fig. 13.

As can be seen from Fig. 13, deviations exist between the experimental and calculated results for each curve. This is because the magnetization degree of the magnetic core continuously changes with the variation of the line current, and its relative permeability is not a fixed value. However, the trends of the experimental and calculated results for each curve are consistent. Although the MFEH can output higher power when the magnetic core is not connected to the EHEHC, the magnetic core enters the saturation state earlier and remains in saturation throughout operation. When the magnetic core is connected to the EFEHC, its current-withstand interval is significantly expanded, and the larger the capacitance of the EFEHC, the wider the linear operating range of the magnetic core becomes. The load output power gradually increases only as the current rises. It can be predicted that when the line current is relatively small, the winding output voltage fails to reach the input threshold of the buck converter. In combination with Fig. 10, the transition diagram between EFEH and MFEH is shown in Fig. 14.

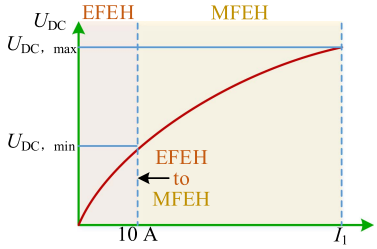

Fig. 14. Transition diagram between EFEH and MFEH.

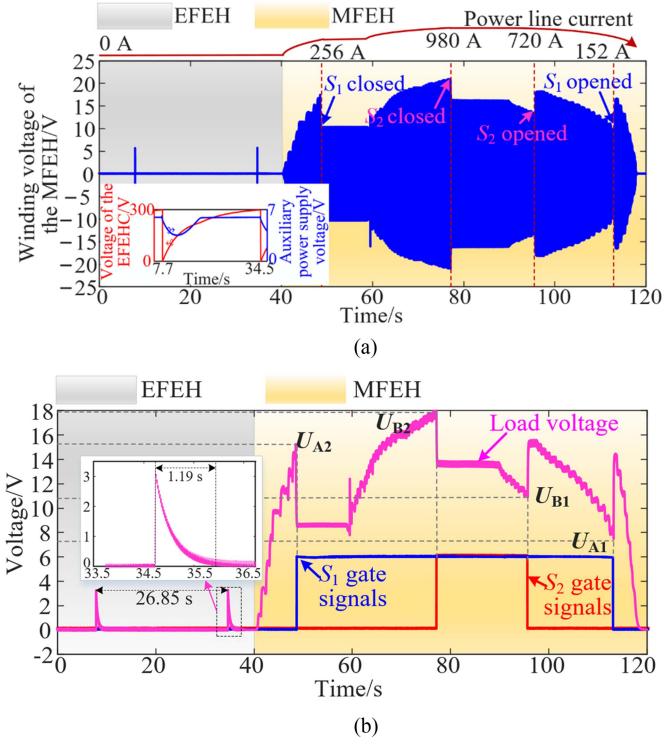

Fig. 15. Experimental waveforms. (a) Voltages of the MFEH winding, the EFEHC, and the auxiliary power supply. (b) Voltages of the load and the gate signals.

Subsequently, experiments are carried out to investigate the transitional energy harvesting between the EFEH and MFEH under conditions of wide current fluctuation ranges. The power line current is gradually adjusted from 0 A to approximately 1000 A and then slowly decreased using the high-current generator. As shown in Fig. 15(a) and (b), the output waveforms of the MFEH winding voltage and load voltage are recorded during this process.

As shown in Fig. 15(a) and (b), the auxiliary power supply of the EFEH operates as intended. Meanwhile, when the magnetic field current is 0 A, the load power primarily originates from the electric field energy. As the line current increases and the load voltage reaches U_{A2} and U_{B2}, the gate-level signals of both S_1 and S_2 are driven to a high logic state, activating their switching functions. This also indirectly verifies the feasibility of the auxiliary power supply of the MFEH. Therefore, the switches S_1 and S_2 are sequentially closed, clamping the load voltage below 18 V. When the power line current decreases from 1000 A,

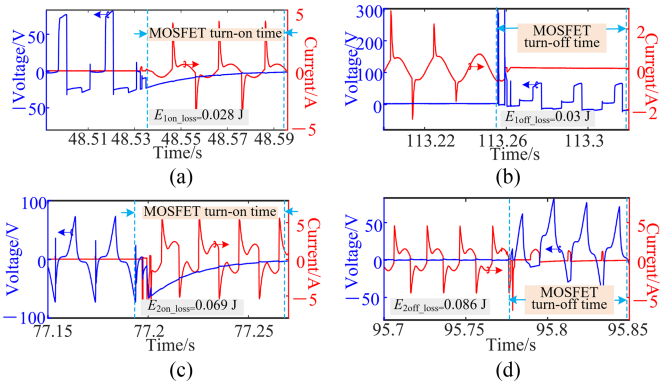

Fig. 16. Switching waveforms. (a) Turn-ON waveform of the MOSFET in S_1. (b) Turn-OFF waveform of the MOSFET in S_1. (c) Turn-ON waveform of the MOSFET in S_2. (d) Turn-OFF waveform of the MOSFET in S_2.

switches S_2 and S_1 open sequentially, allowing the load voltage to recover and ensuring sufficient power delivery. The energy required for adaptive switching of the pulsed EFEH discharge switch, S_1, and S_2 is entirely supplied by the auxiliary power supply, fully aligning with the operational logic of the wide current-range electromagnetic energy integration and handover method. Meanwhile, the average power of EFEH P_{avg} in the current experimental setup can be calculated as follows:

$$P_{avg} = \frac{C_s {U_{DC}}^2}{2t_i} = \frac{2200 \times 10^{-6} \times 3.3^2}{2 \times 26.85} = 0.45\,\text{mW}. \quad (23)$$

Notably, if the initial discharge voltage fails to reach the buck converter startup threshold, the energy accumulation method shown in Fig. 3 can be applied to boost the voltage. Once the MFEHC voltage exceeds the minimum input voltage threshold of the buck converter, the energy is discharged to the load. Alternatively, when the EFEHC is discharged to the MFEHC for the first time and the voltage and energy of the MFEHC are just sufficient to power the load, the employment of a buck converter can be eliminated.

Furthermore, during the MFEH stage, the switching drain-source voltage and current waveforms of a single MOSFET within switches S_1 and S_2 are captured and presented in this article, as illustrated in Fig. 16.

Where E_{1ON_loss} and E_{1OFF_loss} are the turn-ON and turn-OFF losses of the MOSFET for S_1, E_{2ON_loss} and E_{2OFF_loss} are the turn-ON and turn-OFF losses of the MOSFET for S_2. In Fig. 16(a)–(d), the test results conclusively validate that the switchgear maintains uncompromised commutation integrity within ac environments. In other words, the ac switches are capable of reliable turn-ON and turn-OFF operation. Since the power line current is not expected to fluctuate significantly in the short term and the switching frequency is low, the heat generated due to switching losses will not accumulate and can be effectively dissipated. As the two switches are connected to the EFEH winding, the EFEH winding waveforms during switch opening and closing, as well as the harvested energy during the switch ON/OFF periods, are presented in Fig. 17.

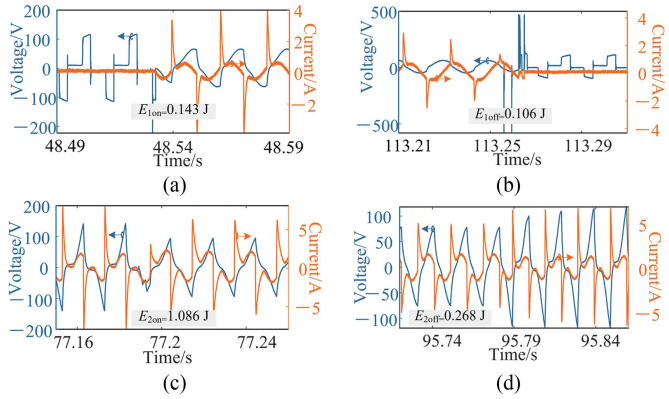

Fig. 17. EFEH winding waveforms. (a) S_1 closed. (b) S_1 opened. (c) S_2 closed. (d) S_2 opened.

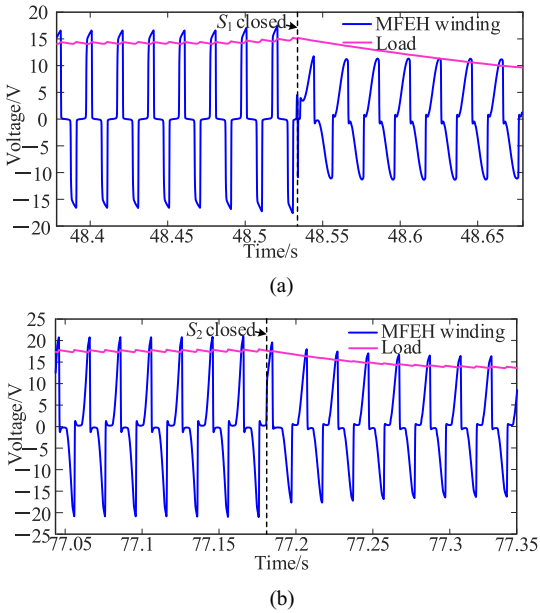

Fig. 18. Voltage waveform before and after switch closure. (a) S_1 closed. (b) S_2 closed.

Where E_{1ON} and E_{1OFF} are the harvested energies from the EFEH winding during the closing and opening of switch S_1. E_{2ON} and E_{2OFF} are the harvested energies from the EFEH winding during the closing and opening of switch S_2. By comparing Figs. 17(a)–(d) with 16(a)–(d) in sequence, it can be seen that the energy harvested by the EFEH winding is greater than the energy required for switch turn-ON/turn-OFF, which further verifies the feasibility of the ac switch operation proposed in this article. To analyze core saturation under different switch states, the waveforms of the MFEH winding voltage and load output voltage during switch transitions are plotted, which are shown in Fig. 18(a) and (b), respectively.

As shown in Fig. 18(a), the instantaneous closure of switch S_1 sharply increases the EFEHC, reducing its impedance. A portion of the magnetic energy flows into the EFEH winding, resulting in a near-sinusoidal waveform for the MFEH winding when the S_1 is closed, indicating significantly reduced core saturation and

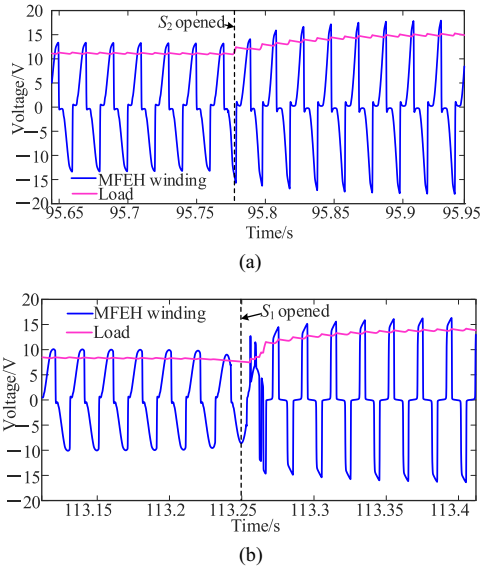

Fig. 19. Voltage waveform before and after the switch opened. (a) S_2 opened. (b) S_1 opened.

effective load voltage regulation. Fig. 18(b) demonstrates that further increasing the line current and closing switch S_2 amplifies the EFEHC, further suppressing MFEH winding voltage spikes and load voltage fluctuations. Additionally, Fig. 19(a) and (b) show the MFEH winding and load voltage waveforms when S_1 and S_2 are opened, respectively.

As shown in Fig. 19(a), with the decrease of the power line current, the disconnection of switch S_2 reduces the EFEHC, increasing its impedance. Magnetic energy flows into the magnetizing resistor, deepening core saturation, but at lower currents, this raises the load output voltage while ensuring it remains below the buck converter's maximum tolerance. Fig. 19(b) reveals that as the power line current continues to decrease, core saturation is alleviated. When S_1 is disconnected, saturation deepens again, but the load voltage rises to prevent it from dropping below the buck converter's minimum input threshold. Furthermore, analysis demonstrates a positive correlation between load output voltage and core saturation depth: higher load voltage corresponds to deeper saturation.

In summary, the proposed wide current-range electromagnetic energy harvesting integration and handover method effectively addresses hybrid electromagnetic energy collection, core saturation control, and load voltage regulation. Through the coupling interaction between the EFEH and MFEH windings, the system achieves adaptive switching of two-stage switches without external power intervention. Under high line currents, it significantly reduces core saturation depth and suppresses voltage spikes, preventing damage to components like the buck converter. Under low line currents, it disconnects EFEH capacitors and elevates the load voltage, ensuring stable power delivery.

VII. Conclusion

This article proposed an efficient electromagnetic energy harvesting integration and handover method for wide current ranges, where the electric field energy storage capacitor was

connected as a capacitive load to the secondary winding of the MFEH circuit, forming a parallel loop with the load. Based on the multiwinding equivalent model, explicit analytical relationships were established among load output voltage, output power, magnetic flux density, line current, load, and the EFEHC. By exploring the coupling interaction between dual windings on the core, the EFEHC effectively regulated load voltage, output power, and magnetic core operating range. This methodology proved applicable to monitoring sensors operating under large current fluctuations with intermittent and real-time modes, offering practical value for self-powered sensor designs in high-voltage power grids.

REFERENCES

[1] J. P. Ram, D. S. Pillai, N. Rajasekar, and S. M. Strachan, "Detection and identification of global maximum power point operation in solar PV applications using a hybrid ELPSO-P&O tracking technique," *IEEE J. Emerg. Sel. Topics Power Electron.*, vol. 8, no. 2, pp. 1361–1374, Jun. 2020.

[2] J. Kan, J. Wang, K. Wang, S. Wang, and Z. Zhang, "Design and characterization of wind energy harvesting from a trajectory-controllable piezoelectric vibrator," *IEEE Sensors J.*, vol. 21, no. 21, pp. 23838–23848, Nov. 2021.

[3] H. O. Tabrizi, H. M. P. C. Jayaweera, and A. Muhtaroğlu, "Fully integrated autonomous interface with maximum power point tracking for energy harvesting TEGS with high power capacity," *IEEE Trans. Power Electron.*, vol. 35, no. 5, pp. 4905–4914, May 2020.

[4] C. Xu, W. Wang, W. Su, M. Duan, and M. Hu, "Anti-saturation and power decoupling control of multiwinding energy harvester based on magnetomotive force compensation," *IEEE Trans. Ind. Inform.*, vol. 19, no. 10, pp. 10555–10563, Oct. 2023.

[5] O. Cetinkaya and O. B. Akan, "Electric-field energy harvesting in wireless networks," *IEEE Wireless Commun.*, vol. 24, no. 2, pp. 34–41, Apr. 2017.

[6] J. C. Rodríguez, D. G. Holmes, B. Mcgrath, and R. H. Wilkinson, "A self-triggered pulsed-mode flyback converter for electric-field energy harvesting," *IEEE J. Emerg. Sel. Topics Power Electron.*, vol. 6, no. 1, pp. 377–386, Mar. 2018.

[7] J. C. Rodríguez, D. G. Holmes, B. P. McGrath, and C. Teixeira, "Energy harvesting from medium voltage electric fields using pulsed flyback conversion," in *Proc. IEEE 8th Int. Power Electron. Motion Control Conf.*, 2016, pp. 3591–3598.

[8] J. Zhang, P. Li, Y. Wen, F. Zhang, and C. Yang, "A management circuit with upconversion oscillation technology for electric-field energy harvesting," *IEEE Trans. Power Electron.*, vol. 31, no. 8, pp. 5515–5523, Aug. 2016.

[9] X. Zeng, Z. Yang, P. Wu, L. Cao, and Y. Luo, "Power source based on electric field energy harvesting for monitoring devices of high voltage transmission line," *IEEE Trans. Ind. Electron.*, vol. 68, no. 8, pp. 7083–7092, Aug. 2021.

[10] O. Menéndez, J. Villacrés, R. G. Rivera, and F. A. Cheein, "Analyzing the capabilities of electric field energy harvesting using natural leaves," *IEEE Access*, vol. 9, pp. 158852–158861, 2021.

[11] Y. Shi, X. Cui, L. Qi, X. Zhang, X. Li, and H. Shen, "A novel energy harvesting method for online monitoring sensors in HVDC overhead line," *IEEE Trans. Ind. Electron.*, vol. 70, no. 2, pp. 2139–2143, Feb. 2023.

[12] R. Moghe, A. R. Iyer, F. C. Lambert, and D. Divan, "A low-cost electric field energy harvester for an MV/HV asset-monitoring smart sensor," *IEEE Trans. Ind. Appl.*, vol. 51, no. 2, pp. 1828–1836, Mar./Apr. 2015.

[13] P. Li, Y. Wen, Z. Zhang, and S. Pan, "A high-efficiency management circuit using multiwinding upconversion current transformer for power-line energy harvesting," *IEEE Trans. Ind. Electron.*, vol. 62, no. 10, pp. 6327–6335, Oct. 2015.

[14] S. Paul, S. Bashir, and J. Chang, "Design of a novel electromagnetic energy harvester with dual core for deicing device of transmission lines," *IEEE Trans. Magn.*, vol. 55, no. 2, Feb. 2019, Art. no. 8000104.

[15] M. J. Vos, "A Magnetic core permeance model for inductive power harvesting," *IEEE Trans. Power Electron.*, vol. 35, no. 4, pp. 3627–3635, Apr. 2020.

[16] Y. Li, N. Duan, Z. Liu, J. Hu, and Z. He, "Impedance-matching-based maximum power tracking for magnetic field energy harvesters using active rectifiers," *IEEE Trans. Ind. Electron.*, vol. 70, no. 10, pp. 10730–10739, Oct. 2023.

[17] M. Delzendeh and H. K. Karegar, "Current transformer saturation compensator by using negative voltage feedback," *IEEE Trans. Power Del.*, vol. 35, no. 3, pp. 1200–1208, Jun. 2020.

[18] Y. Zhuang et al., "Improving current transformer-based energy extraction from AC power lines by manipulating magnetic field," *IEEE Trans. Ind. Electron.*, vol. 67, no. 11, pp. 9471–9479, Nov. 2020.

[19] Y. Li et al., "An effective power improving method of magnetic field energy harvesters using a series-connected capacitor for wireless sensors in smart grids," *IEEE Trans. Power Electron.*, vol. 39, no. 7, pp. 8834–8843, Jul. 2024.

[20] Z. Liu et al., "A novel method for magnetic energy harvesting based on capacitive energy storage and core saturation modulation," *IEEE Trans. Ind. Electron.*, vol. 70, no. 3, pp. 2586–2595, Mar. 2023.

[21] K. Ye et al., "A novel method of maximum power point reaching for magnetic field energy harvesting based on a low-power analog control circuit," *IEEE Trans. Power Electron.*, vol. 39, no. 1, pp. 1888–1897, Jan. 2024.

[22] A. Abramovitz, M. Shvartsas, and A. Kuperman, "Enhanced maximum power point reaching method for passive magnetic energy harvesters operating under low primary currents," *IEEE Trans. Power Electron.*, vol. 39, no. 6, pp. 6619–6623, Jun. 2024.

[23] Z. Liu, Y. Li, N. Duan, and Z. He, "An energy management method for magnetic field energy harvesters under wide-range current in railway electrification systems," *IEEE Trans. Ind. Electron.*, vol. 71, no. 5, pp. 5360–5369, May 2024.

[24] Z. Liu, Y. Li, X. Wen, Z. Hu, H. Yang, and Z. He, "A Maximum-Power-Point tracking method based on constant conduction time control with constant voltage output for magnetic field energy harvesters in the saturated region," *IEEE Trans. Power Electron.*, vol. 39, no. 9, pp. 10716–10720, Sep. 2024.

[25] X. Wang, Y. Xia, G. Shi, H. Xia, Y. Ye, and Z. Chen, "Extensible multi-input synchronous electronic charge extraction circuit based on triple stack resonance for piezoelectric and thermoelectric energy harvesting," *IEEE Trans. Ind. Electron.*, vol. 68, no. 8, pp. 7156–7166, Aug. 2021.

[26] G. Shi, J. Chang, Y. Xia, X. Wang, H. Xia, and Q. Li, "A multisource collaborative energy extraction circuit for vibration, ambient light, and thermal energy with MPPT and single inductor," *IEEE Trans. Ind. Electron.*, vol. 70, no. 6, pp. 5819–5829, Jun. 2023.

[27] W. Wang, C. Xu, C. Zhang, and C. Chen, "Start-up and saturation optimization of high-power energy harvester with compound topologies overhead ac transmission line," *IEEE J. Emerg. Sel. Topics Power Electron.*, vol. 8, no. 4, pp. 3609–3617, Dec. 2020.